Cell Reports

Report

Transient N-6-Methyladenosine Transcriptome Sequencing Reveals a Regulatory Role of m6A in Splicing Efficiency

Graphical Abstract

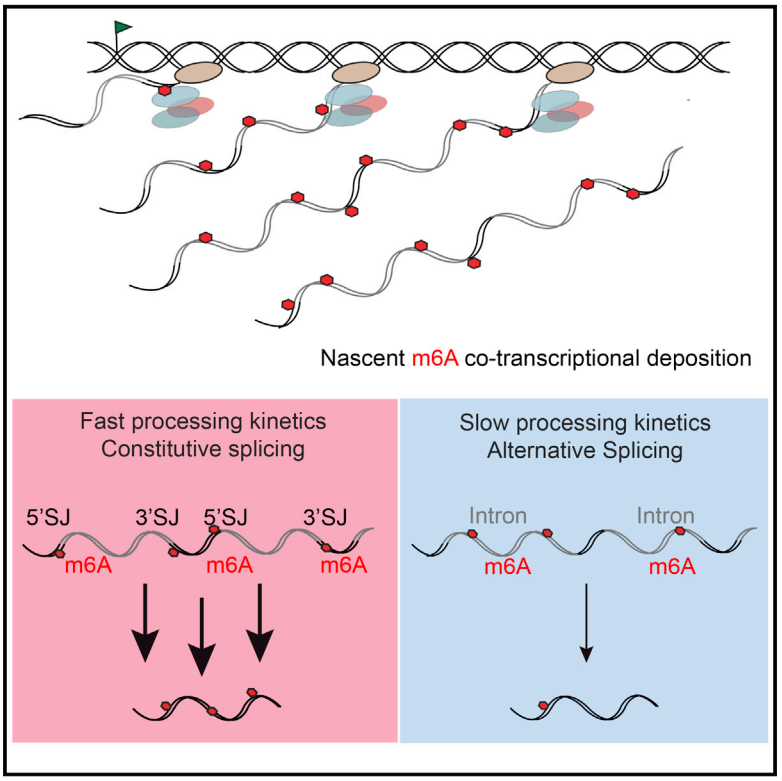

Authors

Annita Louloupi, Evgenia Ntini, Thomas Conrad, Ulf Andersson Vang Ørom

Correspondence

ulf.orom@mbg.au.dk

In Brief

Louloupi et al. describe an approach to detect m6A RNA methylation on nascent RNA. They find that nascent transcripts are often marked by m6A at splice junctions and in introns. The authors show that m6A at splice junctions contributes to faster splicing, while m6A in introns is associated with alternative splicing.

Highlights

- A time-resolved high-resolution picture of m6A on nascent RNA transcripts
- m6A is deposited at nascent RNA and in introns
- m6A deposition at splice-junctions increases splicing kinetics
- High m6A levels in introns is associated with slow and alternative splicing

Data and Software Availability

GSE92565
GSE83561

Louloupi et al., 2018, Cell Reports *23*, 3429–3437
June 19, 2018
https://doi.org/10.1016/j.celrep.2018.05.077

CellPress

Cell Reports
Report

Transient N-6-Methyladenosine Transcriptome Sequencing Reveals a Regulatory Role of m6A in Splicing Efficiency

Annita Louloupi,[1,2,5] Evgenia Ntini,[1,5] Thomas Conrad,[1,3] and Ulf Andersson Vang Ørom[1,4,6,*]
[1]Otto Warburg Laboratories, Max Planck Institute for Molecular Genetics, 14195 Berlin, Germany
[2]Free University, Department of Biology, 14195 Berlin, Germany
[3]BIMSB Genomics, Max Delbrück Center, 13092 Berlin, Germany
[4]Institute for Molecular Biology and Genetics, Aarhus University, 8000 Aarhus, Denmark
[5]These authors contributed equally
[6]Lead Contact
*Correspondence: ulf.orom@mbg.au.dk
https://doi.org/10.1016/j.celrep.2018.05.077

SUMMARY

Splicing efficiency varies among transcripts, and tight control of splicing kinetics is crucial for coordinated gene expression. N-6-methyladenosine (m6A) is the most abundant RNA modification and is involved in regulation of RNA biogenesis and function. The impact of m6A on regulation of RNA splicing kinetics is unknown. Here, we provide a time-resolved high-resolution assessment of m6A on nascent RNA transcripts and unveil its importance for the control of RNA splicing kinetics. We find that early co-transcriptional m6A deposition near splice junctions promotes fast splicing, while m6A modifications in introns are associated with long, slowly processed introns and alternative splicing events. In conclusion, we show that early m6A deposition specifies the fate of transcripts regarding splicing kinetics and alternative splicing.

INTRODUCTION

The RNA nucleotide code is supplemented by more than a hundred chemical modifications, greatly extending the functionality and information content of RNA (Fu et al., 2014; Harcourt et al., 2017). N-6-methyladenosine (m6A) is deposited by a protein complex consisting of the methyltransferase-like 3 and 14 (METTL3 and METTL14), Wilms' tumor 1-associating protein (WTAP), and the Virilizer homolog (KIAA1429) (Liu et al., 2014; Ping et al., 2014; Schwartz et al., 2014). Early studies have demonstrated that adenosine methylation frequently occurs within a subset of RRA*CH consensus sites (R, purine; A*, methylatable A; H, non-guanine base) (Narayan and Rottman, 1988). Fat mass and obesity associated (FTO) and AlkB homolog 5 (ALKBH5) are m6A demethylases, adding dynamics to the function of m6A in RNA biogenesis (Jia et al., 2011; Zheng et al., 2013). m6A is involved in a number of RNA processes, including splicing, RNA degradation, and translation (Bartosovic et al., 2017; Dominissini et al., 2012; Ke et al., 2017; Meyer et al., 2015; Slobodin et al., 2017; Wang et al., 2014; Xiao et al., 2016). These pathways are mediated in part by members of the YTH-domain protein family called m6A readers, which recognize and bind specifically to sequences marked with m6A (Xiao et al., 2016; Xu et al., 2014). The presence of m6A can affect the RNA structure and increase the accessibility of the adjacent RNA sequence for the heterogeneous nuclear ribonucleoproteins HNRNPG and HNRNPC, with an effect on splicing (Liu et al., 2015, 2017). Because of the challenging nature of addressing the impact of m6A on splicing at the mature RNA level, the direct role of m6A on splicing dynamics has not been investigated so far. Here, using TNT-seq (transient N-6-methyladenosine transcriptome sequencing) and qTNTchase-seq (quantitative TNT pulse-chase sequencing), we show that m6A modifications deposited early and co-transcriptionally near splice junctions (SJs) positively affect RNA splicing kinetics. Furthermore, we show that intronic m6A deposition is connected with slow processing kinetics and alternative splicing events. Our results strongly support a scenario where nascent m6A deposition is functionally involved in regulating splicing efficiency (SE) and alternative splicing.

RESULTS

TNT-Seq Reveals m6A Deposition on Newly Transcribed RNA

We developed TNT-seq to identify and study m6A on nascent RNA. In brief, bromouridine (BrU)-labeled RNA was isolated, fragmented, and purified with a BrU-specific antibody. Subsequently, m6A methylated fragments were isolated using an m6A-specific antibody. The labeled RNA (BrU-RNA input) and the m6A-enriched RNA fragments (BrU-m6A-RNA IP eluate) were sequenced to identify positions of m6A on nascent RNA (Figure S1A). We find enrichment of m6A around start and stop codons as well as at 5′ and 3′ SJs reproducibly across independent replicates (Figure S1B), demonstrating a robust experimental pipeline (genome-wide m6A signal correlation = 0.58). The majority (57%) of early m6A peaks (Experimental Procedures) reside within introns, whereas 22% reside in coding sequences (CDSs), 5% are in 5′ UTRs, and 9% are in 3′ UTRs (Figure S1C). To compare m6A peak distribution in newly transcribed RNA with steady-state mRNA, we reanalyzed published m6A-sequencing (m6A-seq)

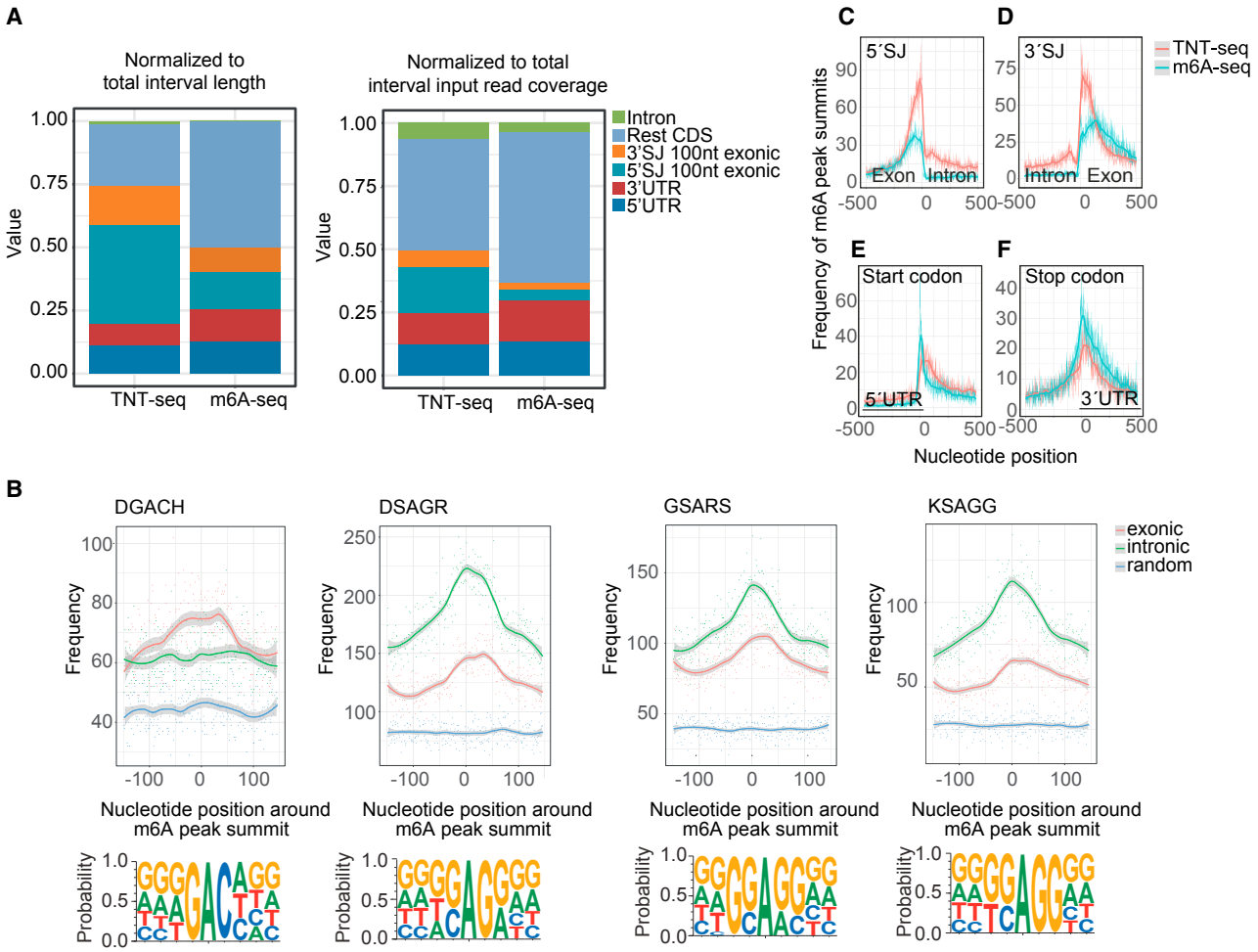

Figure 1. TNT-Seq Reveals m6A Deposition on Newly Transcribed RNA

(A) Distribution of the normalized number of m6A peaks to the length of the analyzed intervals and the respective input read coverage for TNT-seq and mRNA m6A-seq data.

(B) Number of motif occurrences (sum) at nucleotide positions around the m6A peak summit of the top scoring 5,651 exonic peaks, intronic peaks, or random intervals. The line represents loess curve fitting (local polynomial regression), with the 95% confidence interval shaded gray.

(C–F) Distribution (frequency) of the distance of m6A peak summits to the closest given anchor point 5′ SJ (C), 3′ SJ (D), start codon (E), and stop codon (F) for nascent RNA (TNT-seq) and mRNA (m6A-seq; Schwartz et al., 2014).

See also Figure S1.

data (Schwartz et al., 2014) and called m6A peaks using the same pipeline. The majority of steady-state mRNA m6A peaks reside in the CDS (52%), 3′ UTR (28%), and 5′ UTR (12%), while only a minor fraction (4%) is intronic (Figure S1D). Almost half of the CDS-associated nascent m6A peaks reside within 100 nt upstream of the 5′ SJ, and approximately one-fifth are within 100 nt downstream of the 3′ SJ (Figure S1C). For steady-state mRNA, only 17% and 11% of the CDS peaks are within the respective intervals, suggesting a transient functional role of early m6A deposition (Figure S1D). By normalizing the number of m6A peaks to the length of the analyzed intervals and the respective input read coverage, we find that the early m6A deposition is enriched within 100 nt of the 5′ SJ exonic boundary (Figure 1A). To validate the early m6A sites, we assessed the presence of the m6A consensus DRACH motif by performing *de novo* motif search with HOMER (Heinz et al., 2010) in the regions ±150 nt around the peak summit of the top scoring peaks (score >20, n = 5,651) or in randomly generated 300-nt genomic intervals. We find a DGACH motif with a positional enrichment around the peak summit, in particular for exonic peaks (Figure 1B). We also identify three additional motifs sharing an SAG core, with a strong positional enrichment around the peak summit, especially for intronic peaks (Figure 1B). Early m6A deposition is predominant at and in close proximity to SJs (Figures 1C and 1D). In contrast, the picture is inversed around start and stop codons, with a relatively greater number of peaks in steady-state mRNA (Figures 1E and 1F). This finding led us to examine whether early m6A deposition in close proximity to SJs has an impact on splicing of RNA.

m6A Signatures Separate Distinct Intron Classes

To determine the splicing kinetics of newly transcribed RNA, we used BrU-Chase Seq as described previously (Louloupi et al., 2017; Paulsen et al., 2013). Cells were labeled with a 15-min BrU pulse and chased for 0, 15, 30, and 60 min, followed by RNA purification. To determine SE across all time points, we calculated the splicing index value θ (Mukherjee et al., 2017) (Figure 2A), yielding 13,532 introns with an extracted θ value ranging from 0 (unspliced) to 1 (fully spliced). The degree of splicing at 0 min, representing nascent RNA, is lower compared to steady-state chromatin-associated RNA (Conrad et al., 2014), indicating that nascent pre-mRNA is more efficiently captured by our approach than by chromatin fractionation (Figure 2B). Using k-means clustering, we called three clusters of distinct SE dynamics (SED; Experimental Procedures) representing 4,882 fast-, 5,702 medium-, and 2,948 slow-processed introns (Figures 2C–2F). Three representative cases are depicted in Figure 2E. We plotted the average m6A signal per nucleotide position around 5′ and 3′ SJs (Figures 2G–2H) and within length-binned introns for the three groups (Figure S2B). Strikingly, we find that fast-processed introns show greater m6A deposition at SJs, with an overall positive relationship between m6A deposited at 5′ and 3′ SJ exonic boundaries and processing efficiency (Figures 2G–2J and Figures S2A–S2C). By plotting the average frequency of m6A peak summits per nucleotide position (instead of the average m6A signal) for the three subgroups, we reach the same conclusion (Figures S2D–S2F). In contrast, slowly processed introns are associated with increased m6A deposition within the intron (Figures S2B and S2E). To address whether the position of an intron affects m6A signal and SE, we looked at the average m6A signal per nucleotide position around the 5′ and 3′ SJs of only the first and last introns (of transcripts with at least four exons), showing that the effect is independent of the position of the intron (Figures S2G–S2J).

m6A Deposition at Nascent RNA Predicts SED

To further investigate the impact of m6A deposition on nascent RNA in shaping the SED, we used a logistic regression model fit to predict fast- versus slow-processed introns (Figures 2I and 2J). We find that inclusion of the m6A at SJs as an additional parameter improves the predictive power of the model (Figure 2I), with the m6A contribution in predicting fast processing being comparable to other previously shown features, such as the 5′ and 3′ SJ sequence scores and distance to transcription start site (TSS) and transcription end site (TES) (Figure 2J) (Mukherjee et al., 2017). Intron length and internal m6A signal are significantly associated with slow processing (Figure 2J). To complement this analysis, we applied linear regression to predict SED as a continuous value (Figure S3). Again, introducing the m6A at SJs improves the correlation between predicted and measured SED (Figures S3A–S3C), further confirming the impact of early m6A deposition on RNA processing.

Intronic m6A Deposition Associates with Alternative Splicing

We assessed alternative versus constitutive splicing (by extracting the ψ value), as slow pre-mRNA processing has been shown to favor the occurrence of alternative splicing (Mukherjee et al., 2017) (Figure 2A). Alternative splicing events are significantly enriched in slow processed introns (odds ratio, 3.84; Fisher's exact test p value < 2.2e-16) (Figure 3A). Additionally, intronic m6A peaks are associated with upstream or downstream exon skipping approximately two times more often than expected by random chance (odds ratio, 1.7; Fisher's exact test p value < 2.2e-16), suggesting that intronic m6A deposition is involved in alternative splicing. In concurrence, the average m6A signal is greater along alternative versus constitutively spliced introns and the average m6A signal is greater at constitutive versus alternatively spliced SJ exonic boundaries (Figures 3B–3D). The overall intronic m6A, along with the intron length, are significant contributors in determining alternative splicing (Figure 3E). In contrast, m6A at SJ exonic boundaries and strong splice site consensus sequences (SJ score) ensure constitutive splicing (Figure 3E). Inclusion of m6A improves the predictive power of the model fit of constitutive versus alternative splicing (Figure 3F).

Splicing Factors Coincide with m6A Deposition

To investigate how m6A functionality in splicing is mediated, we analyzed available crosslinking immunoprecipitation sequencing (CLIP-seq) data for SRSF factors with an established role in splicing (Xiao et al., 2016). We find that both SRSF3 and SRSF10 show a high probability to have an m6A peak summit in close proximity (<250 nt) (Figures S4A and S4B), with SRSF10 showing relatively greater affinity (Figure S4C). The SAG motif core that we identify in early m6A peaks is reminiscent of the SRSF binding site motifs (Ajiro et al., 2016; Xiao et al., 2016). In addition, both SRSF3 and SFRF10 have been shown to bind near m6A, and while SRSF3 binding is augmented through interaction with YTHDC1, SRSF10 can bind independently to m6A modified regions (Xiao et al., 2016). In agreement with this observation, we find that the ratio of SRSF10/SRSF3 binding is greater at the SJ exonic boundaries for fast-processed introns and internally along within slow-processed introns (Figures S4D–S4F), in concordance with the respective relative enrichment of early m6A deposition (Figures 2G, 2H, and S2). The average ratio of SRSF10/SRSF3 binding clearly separates alternative and constitutive spliced introns (Figures S4G–S4I), most prominently along length-binned introns (Figure S4H). This result is in agreement with the observation that alternative splicing can be antagonistically regulated by SRSF10 versus SRSF3 binding (Xiao et al., 2016). These results suggest that m6A could play a role in shaping the final outcome of splicing through the recruitment of splicing factors with varying m6A affinities.

qTNTchase-Seq Identifies m6A-Marked Fast-Track RNAs

To separate direct m6A-mediated effects on RNA processing from sequence specific ones, we used qTNTchase-seq. Here, BrU-labeled RNA was isolated at 0 and 30 min chase and m6A transcripts were isolated with an m6A-specific antibody without fragmentation. Both supernatant (m6A negative transcripts) and eluate (m6A positive transcripts) were sequenced for each time point to obtain quantitative information, and we calculated the

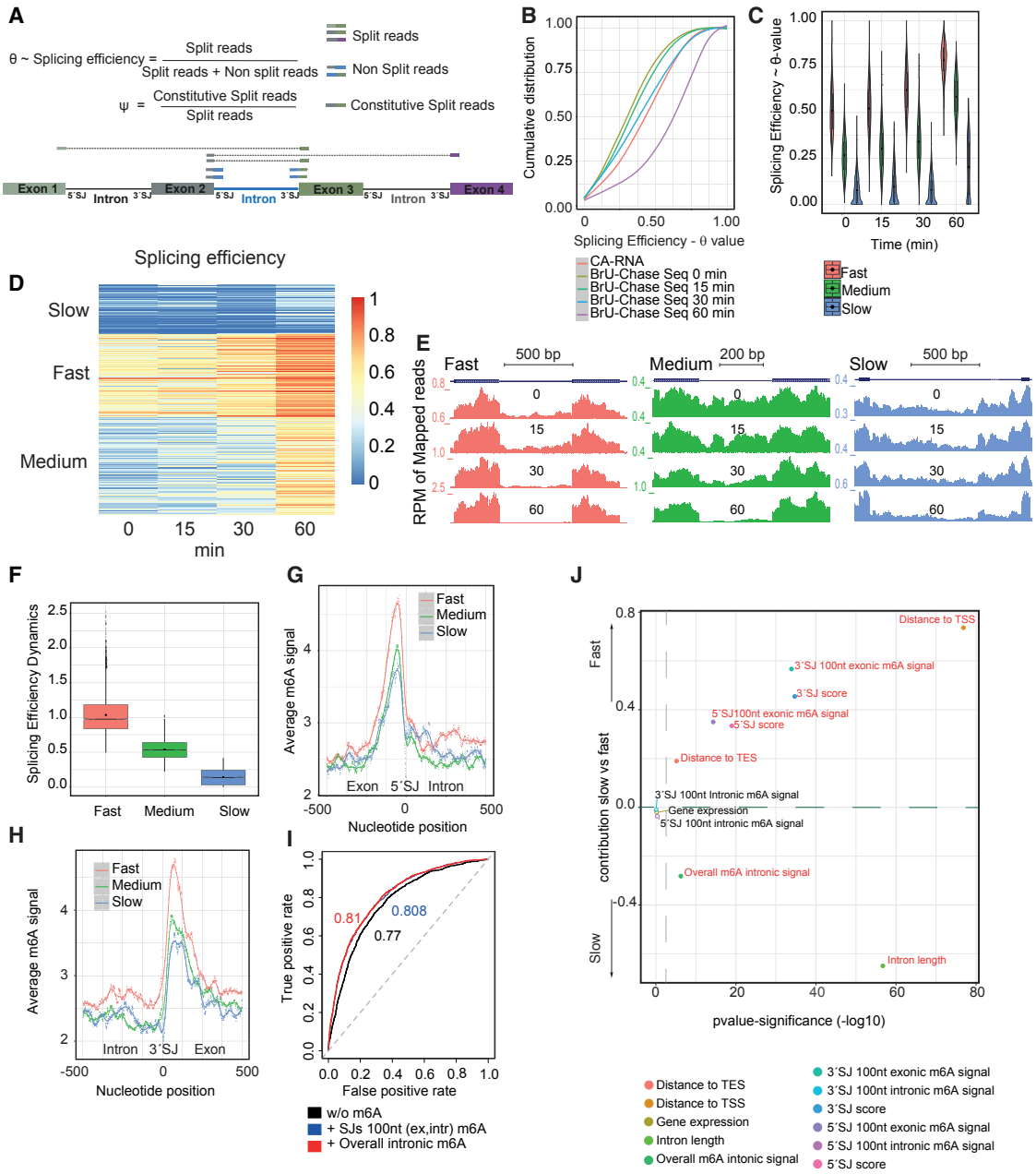

Figure 2. m6A Deposition at Nascent RNA Determines SED

(A) Definition of θ and ψ value.

(B) Cumulative distribution of the SE index from chromatin-associated RNA-seq (Conrad et al., 2014), BrU-Chase Seq (0, 15, 30, and 60 min).

(C) Violin plot representing the density of the SE index (θ value) distribution with embedded box and whisker plots for introns grouped on the basis of differential splicing kinetics.

(D) Heatmap showing the k-means clustering results (with k = 3) of the splicing SE index (θ value) of the 13,532 filtered introns measured for the BrU-Chase time points. Introns are clustered into fast, medium, and slow processed.

(E) UCSC genome browser views of representative cases of introns from each of the three clustering groups.

(F) Boxplot showing distribution of the SED for the fast-, medium-, and slow-processed intron groups.

(G and H) Average m6A signal per nucleotide position in a ±500-nt window around 5′ SJs (G) and 3′ SJs (H) of the filtered introns.

(I) Average receiver-operating characteristic (ROC) curve for discrimination of fast versus slow introns, including all characteristics and excluding m6A. The respective area under the curve (AUC number) is indicated.

(J) Contribution of each feature to the model fit of fast versus slow processing calculated as the coefficients from the binary logistic regression with the associated estimated significance (−log10 p value). The features with p value < 0.001 are colored red.

See also Figures S2–S4.

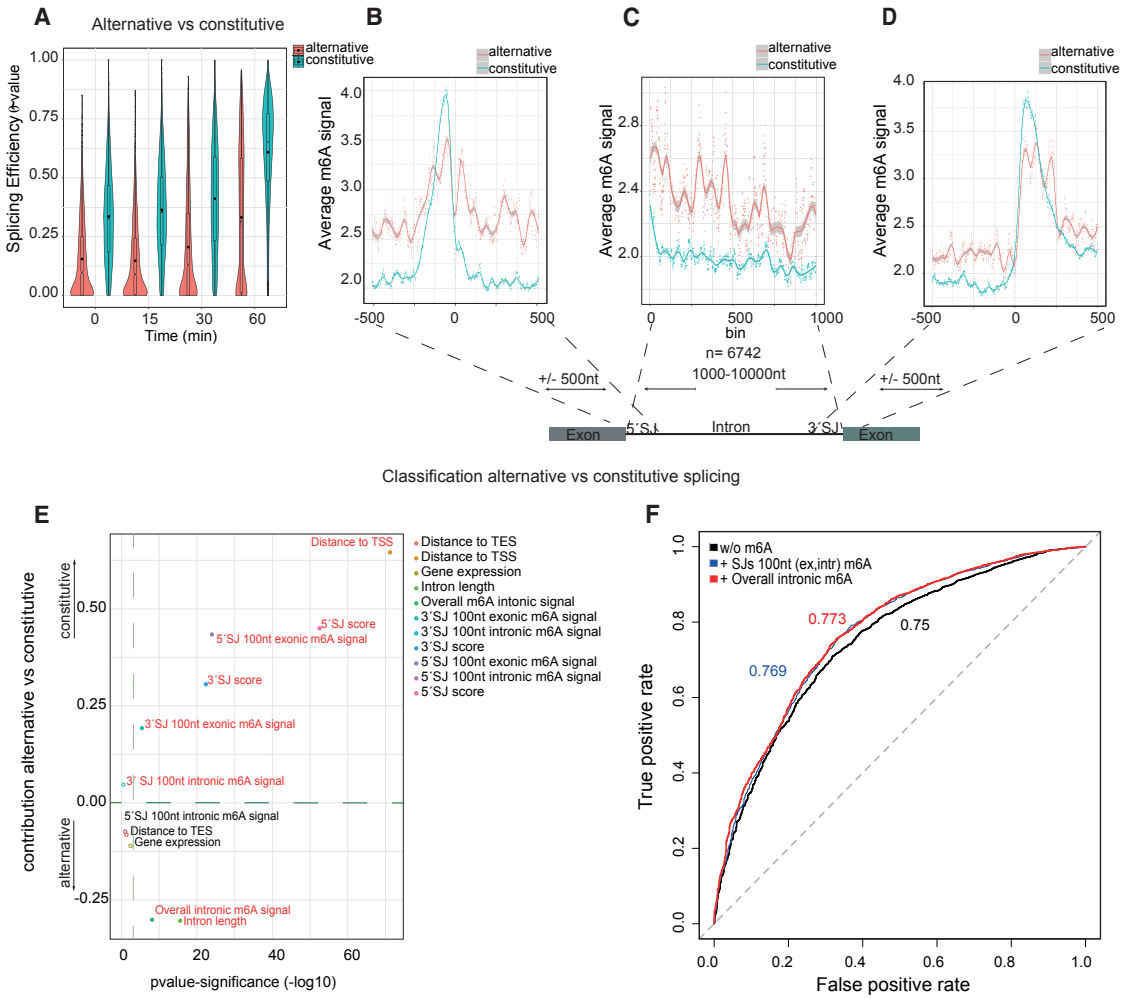

Figure 3. Intronic m6A Deposition Associates with Alternative Splicing

(A) Violin plots showing density of the distribution (with embedded box-and-whiskers plots) of θ value for introns classified as either constitutive or alternative spliced extracted from all pulse-chase time points.

(B–D) Average m6A signal per nucleotide position in a ±500-nt window around the 5′ SJ (B) and 3′ SJ (D) and per bin (C) of 6,742 introns with length 1,000–10,000 nt. The average m6A signal is extracted separately for the two subgroups (constitutive and alternative). The lines represent LOESS curve fitting (local polynomial regression), with the 95% confidence interval shaded gray.

(E) The contribution of each feature to alternative versus constitutive splicing, calculated as the coefficients of the binary logistic regression fit with associated estimated significance (−log10 p value). Features with $p < 0.001$ are colored red.

(F) Average ROC for the logistic regression prediction of the alternative versus constitutive splicing using all features, with and without m6A data. The respective AUC number is indicated.

See also Figure S4.

m6A level per transcript (Molinie et al., 2016). On a transcriptome-wide scale, we observe a strong concordance of m6A levels between biological replicates, both for the top 25% expressed transcripts and for all transcripts with non-zero coverage (0 min: Pearson $r = 0.89$, p value < 2.2e-16; 30 min: Pearson $r = 0.91$, p value < 2.2e-16). The m6A levels do not significantly differ between 0 and 30 min chase, indicating that the overall m6A modification levels of transcripts remain the same for at least ~45 min after transcription (not shown). To follow SE, we extracted the transcript splicing index from m6A-positive and m6A-negative transcripts at 0 and 30 min chase. Within the pulse, corresponding to a 15-min window of transcription, m6A-positive transcripts show significantly higher SE than m6A-negative transcripts (Figure 4A). In addition, by measuring SED at the transcript level, we find that the m6A-positive transcripts show significantly greater processing than their m6A-negative counterparts (two tailed paired *t test* p value < 2.2e-16) (Figure 4B). Importantly, processing appears significantly enhanced for the m6A fraction of individual transcripts; ~76% show gain of SED in the m6A fraction, revealing a direct and sequence-independent impact of m6A on processing kinetics (Figure 4C). We further examined the SE locally for the 13,532

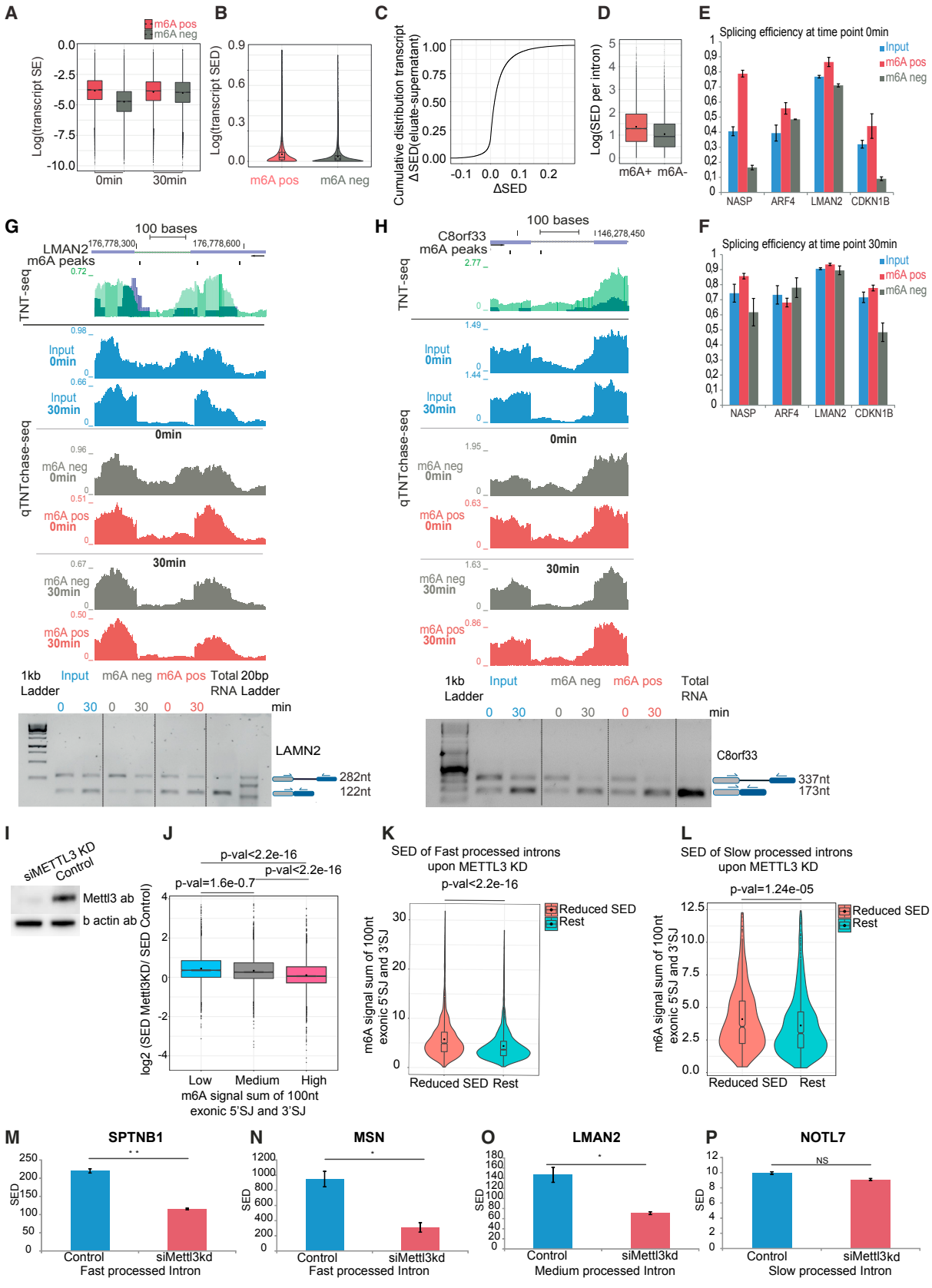

(legend on next page)

filtered introns. We find that ~14% have significantly higher SE in the m6A-positive transcripts and show a 1.26-fold enrichment over random chance to have an m6A peak in the 5′ SJ 250-nt exonic boundary (odds ratio, 1.265; Fisher's exact test *p* value = 0.0006745). In addition, individual intron loci show on average significantly higher SED in the m6A-positive versus m6A-negative transcripts (two-tailed paired t test p value < 2.2e-16) (Figure 4D).

We used qPCR to analyze the splicing kinetics of four candidate SJs that have at least one m6A peak (±250 nt). Strikingly, at time point 0, m6A-positive transcripts show higher SE than the m6A-negative transcripts (Figures 4E and 4F). We confirmed this result with semiquantitative PCR (Figures 4G and 4H).

Nascent m6A Effects Are METTL3 Dependent

To provide a direct link between RNA splicing kinetics and m6A deposition at SJs, we assessed the splicing kinetics after METTL3 knockdown (METTL3 KD) (60 min chase) (Figure 4I). The intron dataset was divided into three equal-size quantiles based on the m6A signal at 5′ and 3′ SJs (5′ and 3′ SJ 100-nt exonic intervals), and the SED was calculated. We plotted the log2 ratio of SED for METTL3 KD to control for introns with low, medium, and high m6A signal (Figure 4J). For introns with high m6A signal on both 5′ and 3′ SJs, we observe a decreased SED upon METTL3 KD for approximately half of the entries (log2 SED ratio METTL3 KD/control < 0) (Figure 4J). For introns with low and medium m6A signal (log2 SED ratio METTL3 KD/control > 0), we observe an increased SED (Figure 4J). The difference in the SED ratio (log2 METTL3 KD/control) of high m6A signal compared to low or medium is significant for both comparisons (t test p value < 2.2e-16). We then focused on fast-processed introns and plotted the m6A signal (sum of 5′ SJ and 3′ SJ 100-nt exonic area) for those that show reduced SED upon METTL3 KD versus the rest (Figure 4K). We find that the METTL3-affected introns have significantly higher m6A at the 5′ and 3′ SJ exonic boundaries. This verifies that the 5′ and 3′ SJ exonic methylation promotes fast splicing kinetics, as also shown by the logistic regression model fit (Figure 2J). We see the same but less pronounced tendency for the slow-processed introns (Figure 4L). qPCR analysis of SED for four candidates confirms the transcriptome-wide data (Figures 4M–4P).

DISCUSSION

We identify an enrichment of m6A deposition near the 5′ SJs of nascent RNA transcripts, and we show that early m6A deposition is associated with distinct RNA processing kinetics. Most importantly, we compare the processing of individual m6A-positive transcripts versus their m6A-negative counterparts, demonstrating that m6A directly controls splicing kinetics irrespectively of the underlying transcript sequence. Our findings suggest that m6A serves as a labeling signal that could be recognized by m6A reader proteins to destine methylated transcripts for specific splicing kinetics. This is in agreement with a study describing m6A methylation as a mark for selective nuclear processing, providing evidence for an m6A-dependent mRNA metabolism (Roundtree et al., 2017).

Our findings furthermore reveal that intronic m6A peaks are enriched in introns involved in alternative splicing. The m6A demethylase FTO binds mostly to introns and mediate removal of m6A. Knockout of FTO causes alternative splicing events with a preference for exon skipping, suggesting that demethylation of mRNA transcripts promotes exon inclusion under normal conditions (Bartosovic et al., 2017). Taken together, these findings suggest that intronic m6A marks that are not targeted or not yet removed by FTO mediate exon skipping, while introns involved in constitutive splicing show no enrichment in the m6A signal and most probably are targets of FTO (Bartosovic et al., 2017). In mRNAs, m6A is enriched in the consensus DRACH motif; however, not all DRACH motifs are methylated, indicating that the presence of the sequence motif alone is not enough to drive m6A deposition. FTO CLIP data show no significant enrichment of the DRACH motif (Bartosovic et al., 2017), leading us to hypothesize that early intronic m6A deposition is mostly in non-DRACH sequences where FTO can detect and eventually remove the m6A marks.

Recently, the m6A reader YTHDC1 was shown to recruit SRSF3 while competing away SRSF10. YTHDC1 binds m6A sites and promote exon inclusion (Xiao et al., 2016). In the absence of YTHDC1 and SRSF3, SRSF10 has the availability to bind to free m6A sites independently, promoting exon skipping. SRSF3 knockdown in U2OS cells has also been shown to cause exon-skipping events (Ajiro et al., 2016). Using *de*

Figure 4. qTNTchase-Seq Identifies m6A-Marked Fast-Track RNAs

(A) Boxplot representing the overall SE of methylated (m6A positive) versus non-methylated (m6A negative) transcripts at time points 0 and 30 min.

(B) Violin plots showing distribution of the transcript SED in m6A-positive and m6A-negative fractions (two-tailed Student's t test p value < 2.2e-16).

(C) Cumulative distribution of transcript SED differences between the methylated and unmethylated state (⊿SED = SED m6A positive − SED m6A negative).

(D) Boxplot displaying SED per intron in m6A-positive and m6A-negative transcripts (two-tailed paired t test p value < 2.2e-16).

(E and F) qPCR analysis of the local intronic SE of methylated versus non-methylated transcripts for 0 min (E) and 30 min (F).

(G and H) UCSC genome browser tracks of qTNTchase-seq data for LMAN2 (G) and C8orf33 (H) representing the transcript regions used for the qRT-PCR analysis. Normalized read coverage (reads per million of total number of mapped reads) tracks for input (blue), supernatant m6A negative (gray), and eluate m6A positive (pink). The upper overlay track represents the TNT-seq with purple for input and green for IP; black rectangles above represent the called m6A peaks. Below tracks for each sample are agarose gels depicting semiquantitative PCR of input, m6A-positive, and m6A-negative samples for 0 and 30 min.

(I) Western blot for METTL3 KD.

(J) Log2 ratio of SED in METTL3 KD to control for introns with low, medium, and high m6A signal at both 5′ and 3′ SJs (100-nt exonic area).

(K) m6A signal at both 5′ SJs and 3′ SJs (100 nt exonic area) for the fast-processed introns that show reduced SED in the METTL3 KD condition versus the rest (two-tailed Student's t test p value < 2.2e-16).

(L) m6A signal at both 5′ SJs and 3′ SJs (100 nt exonic area) for the slow-processed introns that show reduced SED in the METTL3 KD condition versus the rest (two-tailed Student's t test p value < 2.2e-16).

(M–P) qPCR analysis of SED for fast- (M and N), medium- (O), and slow-processed (P) introns (error bars show SD, n = 2 biological replicates (*p < 0.05 and **p < 0.01, two-tailed Student's t test).

novo motif analysis, we identify three additional motifs sharing a SAG core reminiscent of the SRSF binding site consensus, suggesting that m6A could be involved in recruiting splicing factors to control SE and alternative splicing.

The lack of strong consensus sequences at SJs of many introns may be compensated by the presence of m6A that could eventually attract splicing factors to exert their function. Our study shows that the crucial role of m6A on SED as well as on alternative splicing is position dependent. m6A deposited in intronic regions sort transcripts to a slow-track processing pathway and is associated with alternative splicing while m6A deposited at exonic boundaries of SJs sort transcripts to a fast-track processing pathway and constitutive splicing.

EXPERIMENTAL PROCEDURES

Cell Culture and BrU-Chase Sequencing

HEK293 cells were cultured in DMEM growth medium supplemented with 10% fetal bovine serum (FBS) under normal growth conditions (37°C and 5% CO_2). Cells were 70%–80% confluent before addition of BrU. BrU (−5-bromouridine, Santa Cruz Biotechnology catalog number CAS 957-75-5) was added to a final concentration of 2 mM to the medium and cells were incubated at normal growth conditions for 15 min. Cells were washed three times in PBS and either collected directly or chased in conditional medium supplemented with 20 mM uridine (Sigma catalog number U3750-25G) for 15, 30, and 60 min. RNA was purified using TRIzol following the manufacturer's instructions.

TNT-Seq

For one TNT-seq sample, ~25 150-mm plates were used for BrU labeling. RNA was labeled and isolated as described above. RNA concentration was adjusted to 2 μg/μL with nuclease-free water. 18 μL RNA was added to a thin-walled 200-μl PCR tube following the addition of 2 μL 10X fragmentation mixture (100 mM Tris-HCl [pH 7.4] and 100 mM $ZnCl_2$ in nuclease-free water). Distribution of post-fragmentation size (~100 nt) was analyzed using an Agilent 2100 Bioanalyzer with an Agilent RNA 6000 Pico kit according to the manufacturer's instructions. 400–600 μg fragmented BrU-labeled total RNA was used for each BrU immunoprecipitation (IP). BrU-RNA isolation was performed as described above. 5 μg BrU fragmented RNA was used as input for the m6A-IP buffer. An RNA-antibody-beads mixture was incubated for 2 hr at 4°C with gentle rotation in a final volume of 0.8 mL in protein low-binding tubes. Three washing steps were performed with 1X m6A-IPbuffer (1st and 2nd wash) and high-salt m6A-IP buffer (500 mM NaCl, 0.1% Igepal CA-6300, 10 mM Tris-HCl [pH 7.5]) (3rd wash). At the last wash, the protein low-binding tubes were replaced with DNA LoBind tubes. For elution, 80 μL elution buffer (1X m6A-IP buffer + 6.7 mM m6A nucleotides) was added directly on the beads, and the tubes were incubated for 1 hr with continuous shaking (1,100 rpm) at 4°C. After the second round of elution, RNA was ethanol precipitated and resuspended in 15 μL RNase-free water, and the RNA concentration was measured using the Qubit RNA HS Assay Kit as per the manufacturer's instructions.

siRNA Transfection

HEK293 cells were transfected with four different siRNAs targeting METTL3 transcript (Table S1) using HiPerFect Transfection Reagent from QIAGEN. In brief, reverse transfection was performed using 1×10^6 cells for a single 100-mm plate. Cells were seeded in a final 4 mL volume of medium without antibiotics. 12 μL transfection reagent together with siRNAs (25 nM final concentration) was incubated at room temperature (RT) in 1 mL Opti-MEM I Reduced Serum Medium after mixing for 20 min. The transfection complexes were added drop-wise into the plate. 16 hr after transfection, 5 mL cell culture medium was added to each plate. A second transfection was performed 24 hr after the first transfection. After 40 hr, 5 mL cell culture medium was added to each plate. Knockdown efficiency was analyzed with western blot (anti-METTL3 polyclonal antibody; Protein Tech catalog number 15073-1-AP). BrU-Chase Seq samples were prepared 72 hr after the first transfection. The experiments were performed in duplicate.

RNA Sequencing and Data Analysis

For the BrU- Chase Seq, the library preparation was done using the TrueSeq Stranded Total RNA Kit (Illumina). Sequencing was performed on an Illumina HiSeq 2500 instrument to obtain ~200 million reads per sample. For the TNT-Seq, 100 ng of Input BrU-labeled fragmented RNA and 100 ng of TNT-IP eluate RNA were subjected to library preparation following the TruSeq Stranded mRNA Library Preparation Kit instructions with some modifications.

DATA AND SOFTWARE AVAILABILITY

The accession numbers for the BrU-chase-seq, TNT-seq, qTNTchase-seq, and METTL3 KD BrU-chase-seq data reported in this paper are GEO: GSE92565 and GSE83561.

SUPPLEMENTAL INFORMATION

Supplemental Information includes four figures and one table and can be found with this article online at https://doi.org/10.1016/j.celrep.2018.05.077.

ACKNOWLEDGMENTS

E.N. has been funded by a postdoctoral stipend from the Alexander von Humboldt Foundation. Work in the author's laboratory is funded by the German Research Council (DFG), the Alexander von Humboldt Foundation (Sofja Kovalevskaja Award), and the Novo Nordisk Foundation (Hallas Møller Investigator) to U.A.V.Ø.

AUTHOR CONTRIBUTIONS

Conceptualization, A.L., E.N., T.C., and U.A.V.Ø.; Methodology, A.L., E.N., T.C., and U.A.V.Ø.; Investigation, A.L. and E.N.; Validation, A.L; Formal Analysis, Data Curation, Software, E.N.; Writing – Original Draft, Visualization, A.L, E.N., and U.A.V.Ø.; Writing – Review & Editing, A.L., E.N., T.C., and U.A.V.Ø.; Supervision, Funding Acquisition, U.A.V.Ø.

DECLARATION OF INTERESTS

The authors declare no competing interests.

Received: January 10, 2018
Revised: April 30, 2018
Accepted: May 23, 2018
Published: June 19, 2018

REFERENCES

Ajiro, M., Jia, R., Yang, Y., Zhu, J., and Zheng, Z.-M. (2016). A genome landscape of SRSF3-regulated splicing events and gene expression in human osteosarcoma U2OS cells. Nucleic Acids Res. *44*, 1854–1870.

Bartosovic, M., Molares, H.C., Gregorova, P., Hrossova, D., Kudla, G., and Vanacova, S. (2017). N6-methyladenosine demethylase FTO targets pre-mRNAs and regulates alternative splicing and 3′-end processing. Nucleic Acids Res. *45*, 11356–11370.

Conrad, T., Marsico, A., Gehre, M., and Orom, U.A. (2014). Microprocessor activity controls differential miRNA biogenesis In Vivo. Cell Rep. *9*, 542–554.

Dominissini, D., Moshitch-Moshkovitz, S., Schwartz, S., Salmon-Divon, M., Ungar, L., Osenberg, S., Cesarkas, K., Jacob-Hirsch, J., Amariglio, N., Kupiec, M., et al. (2012). Topology of the human and mouse m6A RNA methylomes revealed by m6A-seq. Nature *485*, 201–206.

Fu, Y., Dominissini, D., Rechavi, G., and He, C. (2014). Gene expression regulation mediated through reversible m^6A RNA methylation. Nat. Rev. Genet. *15*, 293–306.

Harcourt, E.M., Kietrys, A.M., and Kool, E.T. (2017). Chemical and structural effects of base modifications in messenger RNA. Nature *541*, 339–346.

Heinz, S., Benner, C., Spann, N., Bertolino, E., Lin, Y.C., Laslo, P., Cheng, J.X., Murre, C., Singh, H., and Glass, C.K. (2010). Simple combinations of lineage-determining transcription factors prime cis-regulatory elements required for macrophage and B cell identities. Mol. Cell *38*, 576–589.

Jia, G., Fu, Y., Zhao, X., Dai, Q., Zheng, G., Yang, Y., Yi, C., Lindahl, T., Pan, T., Yang, Y.-G., and He, C. (2011). N6-methyladenosine in nuclear RNA is a major substrate of the obesity-associated FTO. Nat. Chem. Biol. *7*, 885–887.

Ke, S., Pandya-Jones, A., Saito, Y., Fak, J.J., Vågbø, C.B., Geula, S., Hanna, J.H., Black, D.L., Darnell, J.E., Jr., and Darnell, R.B. (2017). m^6A mRNA modifications are deposited in nascent pre-mRNA and are not required for splicing but do specify cytoplasmic turnover. Genes Dev. *31*, 990–1006.

Liu, J., Yue, Y., Han, D., Wang, X., Fu, Y., Zhang, L., Jia, G., Yu, M., Lu, Z., Deng, X., et al. (2014). A METTL3-METTL14 complex mediates mammalian nuclear RNA N6-adenosine methylation. Nat. Chem. Biol. *10*, 93–95.

Liu, N., Dai, Q., Zheng, G., He, C., Parisien, M., and Pan, T. (2015). N(6)-methyladenosine-dependent RNA structural switches regulate RNA-protein interactions. Nature *518*, 560–564.

Liu, N., Zhou, K.I., Parisien, M., Dai, Q., Diatchenko, L., and Pan, T. (2017). N6-methyladenosine alters RNA structure to regulate binding of a low-complexity protein. Nucleic Acids Res. *45*, 6051–6063.

Louloupi, A., Ntini, E., Liz, J., and Ørom, U.A. (2017). Microprocessor dynamics shows co- and post-transcriptional processing of pri-miRNAs. RNA *23*, 892–898.

Meyer, K.D., Patil, D.P., Zhou, J., Zinoviev, A., Skabkin, M.A., Elemento, O., Pestova, T.V., Qian, S.B., and Jaffrey, S.R. (2015). 5′ UTR m(6)A promotes cap-independent translation. Cell *163*, 999–1010.

Molinie, B., Wang, J., Lim, K.S., Hillebrand, R., Lu, Z.X., Van Wittenberghe, N., Howard, B.D., Daneshvar, K., Mullen, A.C., Dedon, P., et al. (2016). m(6)A-LAIC-seq reveals the census and complexity of the m(6)A epitranscriptome. Nat. Methods *13*, 692–698.

Mukherjee, N., Calviello, L., Hirsekorn, A., de Pretis, S., Pelizzola, M., and Ohler, U. (2017). Integrative classification of human coding and noncoding genes through RNA metabolism profiles. Nat. Struct. Mol. Biol. *24*, 86–96.

Narayan, P., and Rottman, F.M. (1988). An in vitro system for accurate methylation of internal adenosine residues in messenger RNA. Science *242*, 1159–1162.

Paulsen, M.T., Veloso, A., Prasad, J., Bedi, K., Ljungman, E.A., Tsan, Y.C., Chang, C.W., Tarrier, B., Washburn, J.G., Lyons, R., et al. (2013). Coordinated regulation of synthesis and stability of RNA during the acute TNF-induced proinflammatory response. Proc. Natl. Acad. Sci. USA *110*, 2240–2245.

Ping, X.-L., Sun, B.-F., Wang, L., Xiao, W., Yang, X., Wang, W.-J., Adhikari, S., Shi, Y., Lv, Y., Chen, Y.-S., et al. (2014). Mammalian WTAP is a regulatory subunit of the RNA N6-methyladenosine methyltransferase. Cell Res. *24*, 177–189.

Roundtree, I.A., Luo, G.-Z., Zhang, Z., Wang, X., Zhou, T., Cui, Y., Sha, J., Huang, X., Guerrero, L., Xie, P., et al. (2017). YTHDC1 mediates nuclear export of N^6-methyladenosine methylated mRNAs. eLife *6*, e31311.

Schwartz, S., Mumbach, M.R., Jovanovic, M., Wang, T., Maciag, K., Bushkin, G.G., Mertins, P., Ter-Ovanesyan, D., Habib, N., Cacchiarelli, D., et al. (2014). Perturbation of m6A writers reveals two distinct classes of mRNA methylation at internal and 5′ sites. Cell Rep. *8*, 284–296.

Slobodin, B., Han, R., Calderone, V., Vrielink, J.A.F.O., Loayza-Puch, F., Elkon, R., and Agami, R. (2017). Transcription impacts the efficiency of mRNA translation via co-transcriptional N6-adenosine methylation. Cell *169*, 326–337.e12.

Wang, X., Lu, Z., Gomez, A., Hon, G.C., Yue, Y., Han, D., Fu, Y., Parisien, M., Dai, Q., Jia, G., et al. (2014). N6-methyladenosine-dependent regulation of messenger RNA stability. Nature *505*, 117–120.

Xiao, W., Adhikari, S., Dahal, U., Chen, Y.-S., Hao, Y.-J., Sun, B.-F., Sun, H.-Y., Li, A., Ping, X.-L., Lai, W.-Y., et al. (2016). Nuclear m(6)A reader YTHDC1 regulates mRNA splicing. Mol. Cell *61*, 507–519.

Xu, C., Wang, X., Liu, K., Roundtree, I.A., Tempel, W., Li, Y., Lu, Z., He, C., and Min, J. (2014). Structural basis for selective binding of m6A RNA by the YTHDC1 YTH domain. Nat. Chem. Biol. *10*, 927–929.

Zheng, G., Dahl, J.A., Niu, Y., Fedorcsak, P., Huang, C.M., Li, C.J., Vågbø, C.B., Shi, Y., Wang, W.L., Song, S.H., et al. (2013). ALKBH5 is a mammalian RNA demethylase that impacts RNA metabolism and mouse fertility. Mol. Cell *49*, 18–29.